IMPACT OF SYNTHESIS ROUTE ON THE WATER OXIDATION KINETICS OF HEMATITE PHOTOANODES

Camilo A. Mesa,[†]* Ludmilla Steier,[†] Benjamin Moss,[†] Laia Francàs,[†§] James E. Thorne,[†] Michael Grätzel[‡] and James R. Durrant[†]*

[†] Molecular Sciences Research Hub and Centre for Processable Electronics, White City Campus, London W12 0BZ, United Kingdom
[‡] Institut des Sciences et Ingénierie Chimiques, École Polytechnique Fédérale de Lausanne, Station 6, CH-1015 Lausanne, Switzerland

[§]*Current address*: Departament de Química, Universitat Autònoma de Barcelona, Cerdanyola del Vallès, Barcelona 08193, Spain

ABSTRACT

Operando spectroelectrochemical analysis is used to determine the water oxidation reaction kinetics for hematite photoanodes prepared using four different synthetic procedures. Whilst these photoanodes exhibit very different current / voltage performance, their underlying water oxidation kinetics are found to be almost invariant. Lower photoanode performance was found to correlate with the observation of optical signals indicative of charge accumulation in mid-gap oxygen vacancy states, indicating these states do not contribute directly to water oxidation.

Photoelectrochemical water splitting is attracting extensive interest as a promising solar-to-fuel process to store solar energy in chemical bonds (*i.e.*, hydrogen). In solar-driven water splitting, it is widely accepted that the oxygen evolution reaction (OER) is the most kinetically demanding process, especially when using earth abundant metal-oxide photoanodes.[1,2] Consequently, one of the primary limitations to efficiency in such photoanodes is the kinetic mismatch between the lifetimes of photogenerated charges, limited by recombination processes on ps to ms timescales, and the slow kinetics of OER catalysis, occurring usually on the ms – s timescale.[3–5] The efficiency of such photoanodes is strongly dependent on not only the selection of metal oxide, but also the methodology used to synthesize the photoanode, attributed to variations in nanomorphology, surface facet, doping and surface state densities and surface / co-catalyst treatments.[2] However, it is often unclear whether such variations in photoelectrochemical performance result from differences in the underlying kinetics of OER catalysis or rather from differences in competing bulk or surface recombination processes. In this study, we address this issue for one of the most widely studied metal oxides for light driven oxygen evolving photoanodes, hematite (α-Fe_2O_3). The kinetic mismatch between charge recombination and water oxidation is particularly severe in hematite. Consequently, analyzing the connection between overall performance and the underlying OER kinetics in hematite photoanodes synthesized by different deposition methods, yielding different morphologies, may inform strategies to further narrow the kinetic mismatch between reaction and recombination.

One of the key considerations for water oxidation on metal oxides, including hematite, is the potential role of intra-bandgap surface states.[6–9] Such surface states have often been related to oxygen vacancies and structural imperfections / defect sites.[10,11] Surface holes on hematite have been assigned to Fe^{IV}=O species, with these states being proposed as the first intermediate species of the OER.[12] Some studies, including electrochemical impedance analyses, have provided evidence that mid-gap surface states participate as intermediates in the OER catalysis on such photoanodes.[13–16] Other studies, including transient absorption analyses, have suggested OER catalysis is driven by valence band holes localized at the metal oxide surface, with intra-bandgap (e.g.: oxygen vacancy) states primarily function as electron / hole trapping sites, impacting upon bulk and back electron-hole recombination.[6,17–20] The impact of surface states on the water oxidation catalysis on metal-oxide photoanodes such as α-Fe_2O_3 therefore remains controversial.

Herein we employ *operando* spectroelectrochemical analyses to determine the underlying OER kinetics on hematite photoanodes synthesized by four different methodologies. Despite exhibiting very different overall efficiencies for photoelectrochemical water oxidation, the underlying kinetics of water oxidation are almost independent of the synthetic route. In addition, we present evidence of optical signals arising from surface states in less active photoanodes but find that charge accumulation in these states does not drive OER catalysis.

In this study, hematite photoanodes were synthesized and subjected to different post-deposition annealing treatments: (i) 400 nm thick cauliflower Si-doped hematite synthesized by atmospheric pressure chemical vapor deposition (APCVD) at 500 °C,[21,22] (ii) flat 20 nm thick hematite deposited at 230 °C by atomic layer deposition (as-prepared ALD-AP)[23] (iii) identical ALD hematite film annealed at 600 °C (ALD-AN), and (iv) a dense solution-based regrown (SBR) film annealed at 800 °C.[24] For details on the deposition methods and physical characterization, please refer to the SI, Figures S1 to S3. These films exhibit very different morphologies (with for example roughness factors ranging from 21 to 1.2), but all exhibit high crystallinity and the presence of the (110) crystal facet (see Supporting Information Figure S4). In common with many metal oxides, thermal annealing of hematite photoanodes is expected to reduce structural lattice disorder and drive the removal of oxygen vacancies and/or surface states as reported previously.[25–27]

Figure 1 shows the photoelectrochemical performance of the four hematite photoanodes studied herein. It is apparent that the four films exhibit very different *JV* curves (Figures 1.a and 1.b) under 1 sun irradiation conditions (see Figure 1.c and Figure S5 for non-normalized *JV*s). These photoanodes exhibit plateau photocurrent densities from ~0.4 to ~2.7 mA cm^{-2} at 1.5 V *vs* RHE (*i.e.*, bias conditions where no back electron-hole recombination and no dark catalysis occur), in agreement with previous reports in literature.[21,23,24] The two ALD films generate ~ 1 order of magnitude lower photocurrent densities, most likely due to their lower light absorption and lower exposed surface area (roughness factor) compared to the APCVD and SBR films. Figures 1.a and 1.b also show less prominent cathodic current spikes for both SBR (purple) and ALD-AN (red) photoanodes compared to the APCVD (green) and ALD-AP (blue) samples observed under chopped light excitation. Such cathodic spikes have previously been associated with back electron-hole (surface) recombination processes.[20,28,29] Their suppression in the SBR and ALD-AN films correlates with their earlier (less positive) photocurrent onset potentials, < 0.9 V *vs* RHE (see Figure 1.d), with the SBR photoanodes exhibiting an onset of 0.7 V *vs* RHE, close to the state-of-the-art reported for hematite photoanodes without co-catalyst treatments.[24,30,31]

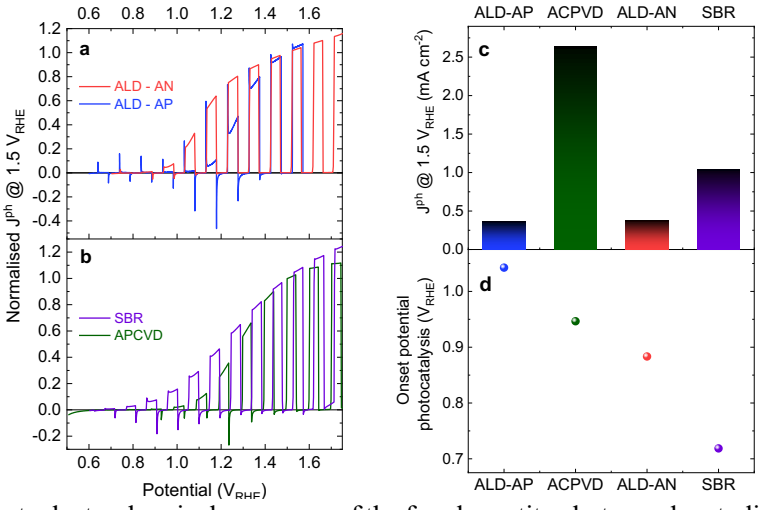

FIGURE 1. Photoelectrochemical responses of the four hematite photoanodes studied herein. Normalized linear sweep voltammetries (10 mV s^{-1}) of the **a)** ALD as-prepared (ALD-AP, blue) and annealed (ALD-AN, red) and **b)** APCVD (green) and solution-based regrown (SBR, purple) hematite photoanodes. Normalization performed at their photocurrent densities at 1.5 V *vs* RHE. **c)** non-normalised current

densities at this 1.5 V bias. **d)** onset potentials for the water oxidation catalysis taken as the applied potential required to reach 1% of the photocurrent densities @ 1.5 V vs RHE. All data collected in three electrode PEC cell under chopped 1 sun illumination in 1 M NaOH.

To determine the underlying OER kinetics on these photoanodes, spectroelectrochemical rate law analyses were employed to determine the reaction orders and water oxidation rate constants (k_{WO}) for each photoanode. These *operando* spectroelectrochemical photo-induced absorption (SEC-PIA) measurements, taken as a function of light intensity, were analyzed using the following equation, in accordance to a procedure previously reported by our group.[32,33]

$$J^{ph} = k_{WO} \cdot (p_s^+)^{\alpha} \qquad \text{Eq. 1}$$

where J^{ph} corresponds to the water oxidation reaction rate, measured by the steady-state photocurrent density and p_s^+ corresponds to the density of surface holes (Fe^{IV}=O states) accumulated at the photoanode surface, as measured by their optical absorbance at 650 nm[32] (this spectral assignment is discussed further below). Log/log plots J^{ph} versus p_s^+ are shown in Figure 2, and allow determination of apparent reaction rate constants, k_{WO} and reaction orders, α with respect to surface hole density. As we have discussed previously, this analysis assumes for simplicity, that all surface valence band holes accumulating under these conditions have similar enthalpies, with increases in water oxidation rate with higher light intensity or more anodic bias being assigned to increases in the density of these species, yielding an increased optical absorption.

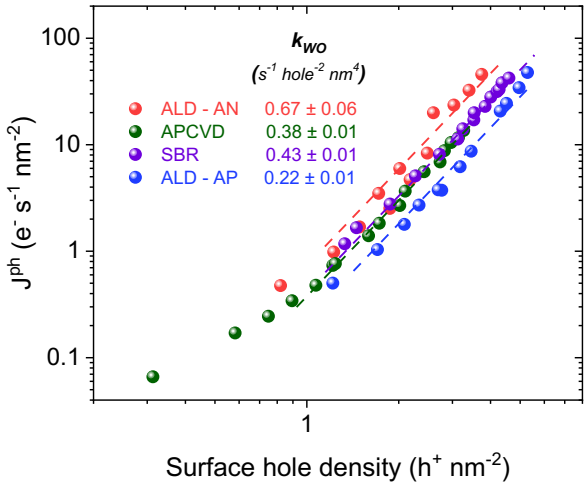

FIGURE 2. Log/log plot of the water oxidation photocurrent density *vs.* the surface hole density measured at 1.5 V *vs.* RHE in 1 M NaOH electrolyte of the APCVD (green), SBR (purple), ALD –AP (blue) and ALD-AN (red) hematite photoanodes. The surface hole density was converted from the optical absorption at 650 nm using a hole extinction coefficient value of 640 M^{-1} cm^{-1} (for details on the extinction coefficient determination, please refer to ESI Figure S6). The data has been corrected for the roughness factor, 1.2 reported for the ALD[23], 21 reported for the APCVD[21] and 1.7 measured herein for the SBR films, measured herein. All dashed lines are fitted to a gradient of 3.

It is apparent from Figure 2 that all four photoanodes show remarkably similar water oxidation reaction kinetics. This contrasts with their markedly different overall *JV* performance (Figure 1). All four photoanodes exhibit a 3rd order of reaction (α ~ 3) with respect to surface hole density (with α determined from the line gradients in Figure 2), as we have previously reported for the APCVD α-Fe_2O_3 film.[32] Such 3rd order behavior has also been observed for $BiVO_4$[34] and TiO_2[35] photoanodes, and has been suggested to be indicative of the rate determining step (RDS) in water oxidation requiring the equilibrium of three surface holes with the reaction center.[36] Third order kinetics are observed for all photoanodes, despite exhibiting turn on potentials differing by up to 200 mV and saturating photocurrent densities ranging by an order of magnitude. Third order rate constants for the OER, k_{WO}, are found to follow the trend ALD-AN>SBR≈APCVD>ALD-AN. Interestingly, such trend coincides

with the observed back electron-hole recombination losses observed in the *JV* curves (Figure 1.a and 1.b).

Figure 2 shows that the ALD-AP photoanode exhibits an approximately three-fold lower k_{WO} than the ALD-AN photoanode. To further investigate this difference, log/log plots of J^{ph} versus p_s^+ were collected as a function of applied potential (Figures 3.a and b and S7). At less positive applied potentials, higher light intensities were required to achieve equivalent photocurrent densities for all four photoanodes, attributed to enhanced recombination losses. However, plots of the accumulated surface hole density (*i.e.* PIA signal at 650 nm) against photocurrent for the three more efficient photoanodes (Figure 3.a and Figure S7) show that observed photocurrent densities are essentially independent of applied potential (a small dependence is observed for the APCVD photoanode, Figure S7). Thus, the differences in *JV* performance apparent in Figure 1 do not result from differences in the underlying OER kinetics, but rather from the differences in their light absorption and charge separation / recombination kinetics as commented above. This striking observation implies that the effect of a more positive applied potential is mainly to improve the ability of the photoanode to accumulate holes at the surface without changing the underlying OER kinetics. This supports the validity of our rate law analysis (Eq. 1), which assumes that the water oxidation flux is primarily determined by the density of accumulated surface Fe^{IV}=O species, rather than changes in the Fe^{IV}=O energetics or changes in potential drops across the depletion / Helmholtz layers. In contrast, for the lower performance ALD-AP photoanodes, Figure 3.b shows a clear bias dependence of photocurrent density versus 650 nm PIA signal. This implies that for matched optical signal amplitudes, the water oxidation flux for this photoanode becomes smaller at less positive potentials, in contrast to the behavior observed for the more efficient photoanodes (Figure 3.a and Figure S7).

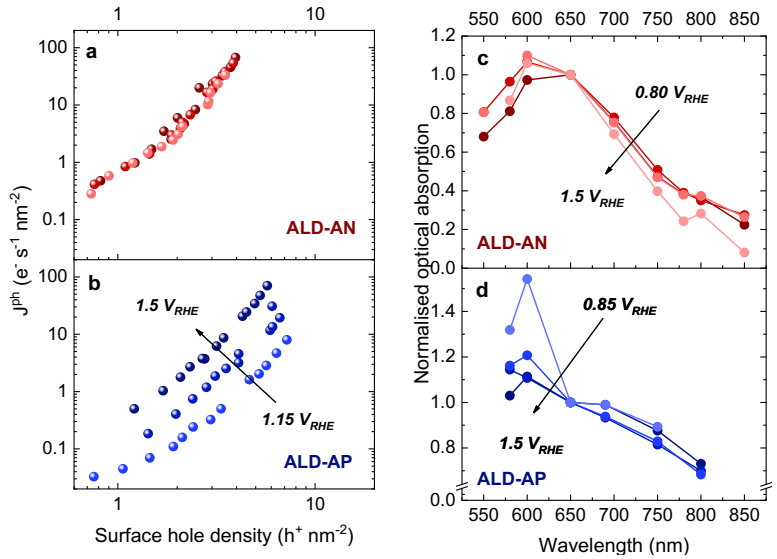

FIGURE 3. Rate law and photo-induced spectra as a function of applied bias for water oxidation on ALD α-Fe_2O_3 photoanodes. Log/log plots of the water oxidation photocurrent density (J^{ph}) *vs.* surface hole density of the **a)** ALD-AN (red) and **b)** ALD-AP (blue) α-Fe_2O_3 films as a function of applied potential (1.15, 1.3 and 1.5 V *vs* RHE). Steady-state PIA spectra of the **c)** ALD-AN (red), measured at 0.8, 1.0, 1.15 and 1.5 V *vs* RHE, and **d)** ALD-AP (blue), measured at 0.85, 1.15, 1.3 and 1.5 V *vs* RHE, α-Fe_2O_3 films under 1 sun illumination in 1 M NaOH.

To further investigate the difference between the ALD-AP and other photoanodes, normalized steady-state PIA spectra are shown in Figure 3.c and 3.d for the ALD-AN and ALD-AP photoanodes respectively, plotted as a function of applied potential at a fixed irradiation intensity (1 sun). The ALD-AN photoanode exhibits a single broad absorption, peaking between 600-650 nm, whose spectral shape is largely independent of applied potential (Figure 3.c). As discussed above, this 650 nm absorption feature has previously been assigned to accumulated surface holes driving water oxidation.[32] This observation indicates that the chemical nature of the holes accumulating under irradiation on these

photoanodes is independent of the applied potential. In contrast, the PIA spectra observed for the ALD-AP photoanodes show an additional narrow, absorbance (Figure 3.d), centered at 580 nm, that becomes relatively more dominant at less positive applied potentials. Analogous, but less pronounced bias dependent PIA spectra were also observed for the APCVD and SBR photoanodes (Figure S7.b). The additional absorption peak resembles a 580 nm spectral feature previously assigned to some extend to oxidation of oxygen vacancy (V_O) states in the space charge layer of APCVD hematite films, and is therefore tentatively assigned to these states. We note that such 580 nm absorption has been alternatively assigned in reference[37] to surface states driving water oxidation. However, a complete study of this spectral feature is beyond the scope of this letter. We also note that the emergence of this spectral feature coincides with a loss of photocurrent density for matched 650 nm absorbance. This can be most readily understood as resulting from the 580 nm absorption feature overlapping with valence band hole absorbance at 650 nm, with these intra-bandgap states not contributing to the OER or photocurrent generation. The PIA data thus indicates that in addition to photoinduced valance band hole accumulation driving water oxidation, the accumulation of oxidized intra-bandgap states in the space charge layer can also be observed. Optical signals from these oxidized states accumulation are most prominent in less efficient photoanodes and at less anodic potentials, indicating such oxidized intra-gap states are relatively inactive in driving water oxidation, but rather act as a photocurrent loss mechanism. The influence of this such parasitic signal in the 650 nm hole absorption, caused by these intra-gap states, can be observed by correlating the transient 650 nm absorption amplitude after 100 ms of a 6 ns laser photoexcitation (see Figure S8 and corresponding discussion in the SI).

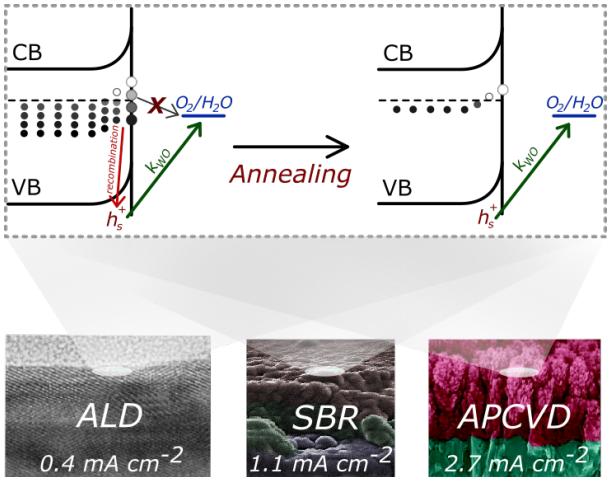

FIGURE 4. Simplified schematic representation water oxidation on the four α-Fe_2O_3 photoanodes studied herein. Filled / empty circles representing reduced / oxidized oxygen vacancy states. Thermally annealing in air is expected to reduce the density of these states, correlated with more efficient water oxidation. See details of HR-TEM and SEM images in Supporting Information Figure S2.

In summary, we find that the kinetics of driving water oxidation by hematite valence band holes are remarkably independent of film synthesis route and nanomorphology, at least for the photoanodes studied herein. This independence is consistent with our previous studies which indicate that the rate determining step for water oxidation on hematite is driven by the localized accumulation of three $Fe^{IV}{=}O$ surface holes, without the need for the presence of specific catalytic sites.[36] As such, differences in photoelectrochemical OER performance of these photoanodes does not derive primarily for differences in OER kinetics, but rather from differences in light absorption and competing charge recombination/trapping pathways. In addition, as illustrated in Figure 4, for less anodic applied potentials, optical signals can be observed in three of our studied photoanodes, indicative of charge accumulation in intra-bandgap states. Charge accumulation in such intra-bandgap states has previously been reported for hematite in several studies, and proposed to drive water oxidation.[13–16] In contrast, the data herein shows that charge accumulating in these states does not contribute significantly to water oxidation, most likely due to their modest oxidation potentials relative to hematite's valence band. These intra-bandgap states have been suggested to be catalytically inactive,[38] instead, they are likely involved in competing trapping processes that can be mitigated with increasing applied potentials.

These intra-bandgap states have been shown by photoelectrochemical impedance spectroscopy means to correlate with the photocurrent onset potential, on ultraspray pyrolysis hematite, upon their oxidation by increasing the applied potential.[39] The presence of such mid-gap states results in apparent potential dependence of kinetics of water oxidation (due to increased charge accumulation in these inactive states at lower potentials); in the absence of such states, the water oxidation rate constant is independent of applied potential. Our results also confirm that on efficient photoelectrodes, the acceleration of water oxidation kinetics at high light levels is determined by surface valence band hole accumulation rather than changes in potential drops across the depletion or Helmholtz layers. Mid-gap states are associated with surface (back electron/hole) recombination losses, as illustrated in Figure 4, and supported by more prominent cathodic current spikes in Figure 1 and consequently more positive photocurrent onset potentials. In summary, we conclude that the primary determinant of water oxidation flux, independent of photoanode synthesis route and applied bias, is the density of $Fe^{IV}=O$ holes accumulated at the photoanode surface.

ASSOCIATED CONTENT

Details on the hematite photoanodes synthesis, UV-Vis spectra, SEM and XRD characterization, Roughness factor determination, PEC characterization details, SEC-PIA and TAS details and supporting figures are provided in the Supporting Information

CORRESPONDING AUTHORS

Camilo A. Mesa, cam111@imperial.ac.uk
James R. Durrant, j.durrant@imperial.ac.uk

NOTES

The authors declare no competing financial interests.

ACKNOWLEDGEMENTS

J.R.D., C.A.M. and L.F. acknowledge the EU (732840 A-LEAF) and J.R.D. additionally thanks EPSRC for funding, C.A.M also thanks the Colombian Science Ministry (former COLCIENCIAS, call 568) for funding. M. G. acknowledges the support from the Swiss National Science Foundation (project 140709) and Swiss Federal Office for Energy (project PECHouse 3; contract no. SI/500090–03).

REFERENCES

(1) Lewis, N. S.; Nocera, D. G. *Proc. Natl. Acad. Sci. U. S. A.* **2006**, *103* (43), 15729.
(2) Kang, D.; Kim, T. W.; Kubota, S. R.; Cardiel, A. C.; Cha, H. G.; Choi, K.-S. *Chem. Rev.* **2015**, *115* (23), 12839.
(3) Peter, L. *J. Solid State Electrochem.* **2013**, *17* (2), 315.
(4) Cowan, A. J.; Durrant, J. R. *Chem. Soc. Rev.* **2013**, *42* (6), 2281.
(5) Klotz, D.; Grave, D. A.; Rothschild, A. *Phys. Chem. Chem. Phys.* **2017**, *19* (31), 20383.
(6) Zachäus, C.; Abdi, F. F.; Peter, L. M.; Van De Krol, R. *Chem. Sci.* **2017**, *8*, 3712.
(7) Klahr, B.; Gimenez, S.; Fabregat-Santiago, F.; Hamann, T.; Bisquert, J. *J. Am. Chem. Soc.* **2012**, *134* (9), 4294.
(8) Thorne, J. E.; Jang, J.-W.; Liu, E. Y.; Wang, D. *Chem. Sci.* **2016**, *7*, 3347.
(9) Grave, D. A.; Yatom, N.; Ellis, D. S.; Toroker, M. C.; Rothschild, A. *Adv. Mater.* **2018**, 1706577.
(10) Le Formal, F.; Tètreault, N. T.; Cornuz, M.; Moehl, T.; Grätzel, M.; Sivula, K. *Chem. Sci.* **2011**, *2* (737–743).
(11) He, Y.; Hamann, T.; Wang, D. *Chem. Soc. Rev.* **2019**, *48* (7), 2182.
(12) Zandi, O.; Hamann, T. W. *Nat. Chem.* **2016**, *8*.
(13) Klahr, B.; Gimenez, S.; Fabregat-Santiago, F.; Bisquert, J.; Hamann, T. W. *Energy Environ.*

Sci. **2012**, *5*, 7626.
(14) Cummings, C. Y.; Marken, F.; Peter, L. M.; Wijayantha, K. G. U.; Tahir, A. A. *J. Am. Chem. Soc.* **2012**, *134*, 1225.
(15) Lv, X.; Rodriguez, I.; Hu, C.; Shang, J.; Sit, P. H. L.; Ye, C.; Oskam, G.; Teoh, W. Y. *Mater. Today Chem.* **2019**, *12*, 7.
(16) Zhang, S.; Shangguan, P.; Tong, S.; Zhang, Z.; Leng, W. *J. Phys. Chem. C* **2019**, *123*, 24352.
(17) Li, W.; He, D.; Sheehan, S. W.; He, Y.; Thorne, J. E.; Yao, X.; Brudvig, G. W.; Wang, D. *Energy Environ. Sci.* **2016**, *9* (9), 1794.
(18) Gurudayal; Peter, L. M.; Wong, L. H.; Abdi, F. F. *ACS Appl. Mater. Interfaces* **2017**, *9*, 41265.
(19) Barroso, M.; Mesa, C. A.; Pendlebury, S. R.; Cowan, A. J.; Hisatomi, T.; Sivula, K.; Grätzel, M.; Klug, D. R.; Durrant, J. R. *Proc. Natl. Acad. Sci.* **2012**, *109* (39), 15640.
(20) Le Formal, F.; Pendlebury, S. R.; Cornuz, M.; Tilley, S. D.; Grätzel, M.; Durrant, J. R. *J. Am. Chem. Soc.* **2014**, *136* (6), 2564.
(21) Kay, A.; Cesar, I.; Grätzel, M. *J. Am. Chem. Soc.* **2006**, *128* (49), 15714.
(22) Cornuz, M.; Grätzel, M.; Sivula, K. *Chem. Vap. Depos.* **2010**, *16* (10–12), 291.
(23) Steier, L.; Luo, J.; Schreier, M.; Mayer, M. T.; Sajavaara, T.; Grätzel, M. *ACS Nano* **2015**, *9* (12), 11775.
(24) Jang, J.-W.; Du, C.; Ye, Y.; Lin, Y.; Yao, X.; Thorne, J.; Liu, E.; Mcmahon, G.; Zhu, J.; Javey, A.; Guo, J.; Wang, D. *Nat. Commun.* **2015**, *6*.
(25) Zandi, O.; Hamann, T. W. *J. Phys. Chem. Lett.* **2014**, *5*, 1522.
(26) Corby, S.; Francàs, L.; Kafizas, A.; Durrant, J. R. *Chem. Sci.* **2020**, *11*, 2907.
(27) Bedoya-Lora, F. E.; Hankin, A.; Holmes-Gentle, I.; Regoutz, A.; Nania, M.; Payne, D. J.; Cabral, J. T.; Kelsall, G. H. *Electrochim. Acta* **2017**, *251*, 1.
(28) Cummings, C. Y.; Marken, F.; Peter, L. M.; Tahir, A. A.; Wijayantha, K. G. U. *Chem. Commun.* **2012**, *48* (14), 2027.
(29) Peter, L. M.; Gurudayal; Wong, L. H.; Abdi, F. F. *J. Electroanal. Chem.* **2018**, *819*, 447.
(30) Young Kim, J.; Magesh, G.; Hyun Youn, D.; Jang, J.-W.; Kubota, J.; Domen, K.; Sung Lee, J. *Sci. Rep.* **2013**, No. 2681.
(31) Hwa Jeon, T.; Moon, G.; Park, H.; Choi, W. *Nano Energy* **2017**, *39*, 211.
(32) Le Formal, F.; Pastor, E.; Tilley, S. D.; Mesa, C. A.; Pendlebury, S. R.; Grätzel, M.; Durrant, J. R. *J. Am. Chem. Soc.* **2015**, *137* (20), 6629.
(33) Francàs, L.; Mesa, C. A.; Pastor, E.; Le Formal, F.; Durrant, J. R. In *Advances in Photoelectrochemical Water Splitting: Theory, Experiment and Systems Analysis*; Tilley, S. D., Lany, S., van de Krol, R., Eds.; The Royal Society of Chemistry, 2018.
(34) Ma, Y.; Mesa, C. A.; Pastor, E.; Kafizas, A.; Francàs, L.; Le Formal, F.; Pendlebury, S. R.; Durrant, J. R. *ACS Energy Lett.* **2016**, No. 1, 618.
(35) Kafizas, A.; Ma, Y.; Pastor, E.; Pendlebury, S. R.; Mesa, C.; Francà, L.; Le Formal, F.; Noor, N.; Ling, M.; Sotelo-Vazquez, C.; Carmalt, C. J.; Parkin, I. P.; Durrant, J. R. *ACS Catal.* **2017**, *7* (7), 4896.
(36) Mesa, C. A.; Francàs, L.; Yang, K. R.; Garrido-Barros, P.; Pastor, E.; Ma, Y.; Kafizas, A.; Rosser, T. E.; Mayer, M. T.; Reisner, E.; Grätzel, M.; Batista, V. S.; Durrant, J. R. *Nat. Chem.* **2020**, *12*, 82.
(37) Klahr, B.; Hamann, T. *J. Phys. Chem. C* **2014**, *118* (19), 10393.
(38) Lewis, N. S. *J. Phys. Chem. B* **1998**, *102* (25), 4843.
(39) Steier, L.; Herraiz-Cardona, I.; Gimenez, S.; Fabregat-Santiago, F.; Bisquert, J.; Tilley, S. D.; Grätzel, M. *Adv. Funct. Mater.* **2014**, *24* (48), 7681.